Geomechanics and Engineering, *Vol. 30, No. 1 (2022) 93-105*
https://doi.org/10.12989/gae.2022.30.1.093

Simulation study on the mechanical properties and failure characteristics of rocks with double holes and fractures

Haiyang Pan[1,2,3], Ning Jiang*[1,2,3], Zhiyou Gao[2,4], Xiao Liang[4] and Dawei Yin[1,2]

[1]*State Key Laboratory of Mine Disaster Prevention and Control, Shandong University of Science and Technology, Qingdao 266590, China*
[2]*College of Energy and Mining Engineering, Ministry of Education, Shandong University of Science and Technology, Qingdao 266590, China*
[3]*General Institute of Exploration and Research of China National Administration of Coal Geology, Beijing 10039, China*
[4]*Shandong Geology and Mineral Resources Engineering Group Co., Ltd. Jinan 250013, China*

(Received December 26, 2021, Revised May 16, 2022, Accepted May 26, 2022)

Abstract. With the exploitation of natural resources in China, underground resource extraction and underground space development, as well as other engineering activities are increasing, resulting in the creation of many defective rocks. In this paper, uniaxial compression tests were performed on rocks with double holes and fractures at different angles using particle flow code (PFC2D) numerical simulations and laboratory experiments. The failure behavior and mechanical properties of rock samples with holes and fractures at different angles were analyzed. The failure modes of rock with defects at different angles were identified. The fracture propagation and stress evolution characteristics of rock with fractures at different angles were determined. The results reveal that compared to intact rocks, the peak stress, elastic modulus, peak strain, initiation stress, and damage stress of fractured rocks with different fracture angles around holes are lower. As the fracture angle increases, the gap in mechanical properties between the defective rock and the intact rock gradually decreased. In the force chain diagram, the compressive stress concentration range of the combined defect of cracks and holes starts to decrease, and the model is gradually destroyed as the tensile stress range gradually increases. When the peak stress is reached, the acoustic emission energy is highest and the rock undergoes brittle damage. Through a comparative study using laboratory tests, the results of laboratory real rocks and numerical simulation experiments were verified and the macroscopic failure characteristics of the real and simulated rocks were determined to be similar. This study can help us correctly understand the mechanical properties of rocks with defects and provide theoretical guidance for practical rock engineering.

Keywords: failure modes; laboratory experiment; mechanical properties; PFC2D; uniaxial compression

1. Introduction

With the development of natural resources in China, underground resource exploitation (Estrada and Bhamidimarri 2016, Chung *et al.* 2019, Tan *et al.* 2022) and underground space development, as well as other engineering activities are increasing. Most of these engineering activities are closely related to rocks (Yin *et al.* 2021, Tan *et al.* 2022, Nicksiar and Martin 2014). Rock is the aggregation of various minerals in nature and the product of natural geological action; rock mass is a geological body, which has experienced repeated geological processes. Structure (rock) is a basic component of the rock mass. Based on the long-term development of geological structures, there are inevitably various defects in rocks, among which holes and cracks are particularly common (Mohammadi and Tavakoli 2015, Wang *et al.* 2020, Zhao *et al.* 2016). Various hole-crack combination defects in rocks will have different effects on the mechanical properties and failure characteristics of the rocks, and such defects lead to a decrease in rock strength (Tan *et al.* 2021, Usol'Tseva 2021, Bahaaddini and Sharrock 2013). Therefore, it is of great significance to study the mechanical properties and failure characteristics of cavity-fractured rocks for practical rock engineering.

To understand the mechanical properties and failure laws of various defective rocks, many scholars have performed significant research on the location, distribution characteristics, number, and combination of holes and cracks. Wang *et al.* (2020) conducted uniaxial compression tests on red sandstone with different defect angles. The acoustic emission method was used to monitor the physical characteristics of energy released during the failure process of the jointed rock mass. The failure mode and energy released by rocks with different defect angles were also different. Chen *et al.* (2020) used numerical simulation software (PFC2D) to conduct uniaxial compression tests on rock masses with various types of hole defects and analysed their failure behaviour and mechanical properties. Li *et al.* (2018) conducted dynamic impact tests on rectangular marble specimens with defects and studied the dynamic mechanical properties and fracture behaviours of marble specimens with single cracks and double cracks in Split-Hopkinson pressure bar tests. Li *et al.* (2019) conducted fatigue loading tests on rock-like specimens with defects

*Corresponding author, Ph.D.
E-mail: jiangning@sdust.edu.cn

ISSN: 2005-307X (Print), 2092-6219 (Online)

using an electro-hydraulic servo fatigue testing machine, in addition, ultrasonic data were collected and analyzed using a digital ultrasonic instrument, and the fatigue damage of defective rock masses under dynamic loading and its influencing factors were investigated. Zhang *et al.* (2018) studied double-hole defect rocks with different central connection angles, and the mechanical behavior and acoustic emission characteristics of rock are systematically analyzed. Zhu *et al*. (2018) studied the influence of arc angles on the mechanical properties, failure modes, and fracture evolution of sandstone through uniaxial compression tests. They determined that during the loading process of sandstone, the bearing capacity of the rock and the number of cracks gradually decrease with an increase in the arc angle of the cracks. Zhu *et al*. (2018) used three-dimensional printing technology and three-dimensional numerical simulations combined with X-ray computed tomography, to capture internal defects in rock and study the mechanical and fracture behaviors of defective rock. Zeng *et al*. (2018) studied the mechanical properties and cracking behaviour of rock specimens with holes under uniaxial compression loading through laboratory tests and two-dimensional particle flow code (PFC2D), and obtained the force field distribution before and during cracking. Li *et al.* (2017) conducted laboratory experiments on dolomite-containing cracks. The wave velocity and open porosity of rock samples were determined through acoustic velocity measurements and natural water absorption tests. A series of uniaxial compression tests were conducted by using a rock mechanical stiffness servo testing system. The strength, deformation characteristics, and failure modes of the rock were analyzed.

Regarding composite defects, Wang *et al*. (2021) used PFC2D to study rock with composite defects consisting of cracks and holes, established single-hole and double-crack combination models at different angles and studied the crack development law and acoustic emission characteristics of different defect combination models. Wu *et al.* (2020) studied the influence of different horizontal distances between holes and crack centers on the mechanical properties of defective rock materials through laboratory experiments and numerical simulations. The results revealed that the peak strength, peak strain, and elastic modulus decrease monotonically and nonlinearly with an increase in the horizontal distance between holes and fractures centers. Li *et al*. (2019) studied the effects of interactions between voids and fissures on the mechanical properties of rocks under uniaxial compression and simulated the crack evolution of such rocks using PFC2D. Wang *et al.* (2018) employed PFC2D to establish models of defective coal and rock samples with different cracks and holes. The stress-strain characteristics and crack evolution law of defective coal and rock samples with different dip angles and holes in different positions were analyzed, and the mechanical properties and crack evolution characteristics of the coal and rock samples were obtained.

Various scholars have performed significant research on the mechanical properties of rocks with single defects and simple fracture combination defects, but there have been few studies on the mechanical characteristics of rocks with double holes and fractures combination defects. In real environments, most rock defects are complex and diverse. Typically, there are different combinations of defects with different angles. To understand the mechanical characteristics of rocks with hole-fracture combination defects, we studied the mechanical properties, failure characteristics, and stress evolution of rocks with double holes and fractures at different angles using PFC2D and laboratory tests. The research on the rocks with double holes and fractures can improve the understanding of the failure mechanism of underground rock engineering.

2. Model establishment and parameter selection

2.1 Determination of particle flow code and parameters

2.1.1 Particle flow code

The particle flow code (PFC) is a numerical simulation (Wang *et al*. 2021) software package developed by Itasca (Cundall and Strack 1979, Cho *et al.* 2007) in the United States. Its theoretical basis is the discrete element method proposed by Cundall and Strack. This software mainly analyses the mechanical properties of rocks using a similar simulation theory. PFC analyses the mechanical properties of a medium from a microscopic perspective, mainly focusing on particles and bonds. Bonds are divided into contact bonds and parallel bonds, which can be used to simulate the connection between particles in rocks. A contact bond has almost no resistance to the force between particles. When the tensile stress and shear stress of the parallel bonds between particles exceed their tensile shear strength, the parallel bonds will break and can transfer force and torque better, as shown in Fig. 1. Parallel bonds can transfer forces and moments between particles, while contact bonds can only transfer forces acting at the point of contact and cannot transfer moments. In this study, a uniaxial compression model for specimens with double holes and fractures at different angles was established by using parallel bonds, and the model was analysed through simulations.

2.1.2 Determination of parameters

Many microscopic parameters are considered when PFC2D is used for numerical simulations of defective rocks, but the microscopic parameters from our laboratory physical experiments cannot be used directly. It is necessary to check and verify the microscopic parameters, such that the numerical simulations are consistent with the data obtained from the laboratory physical experiments. To make numerical simulations more similar to laboratory physical tests, the ‘trial and error method’ is usually used to adjust the microscopic parameters (Lisjak and Grassell 2014, Wang 2016).

Fig. 2 presents a comparison of the final calibration results between the laboratory tests and numerical simulations. It can be observed that the shapes of the stress-strain curves are similar and the failure modes are in good agreement. Therefore, the final microscopic parameters can be determined, as shown in Table 1.

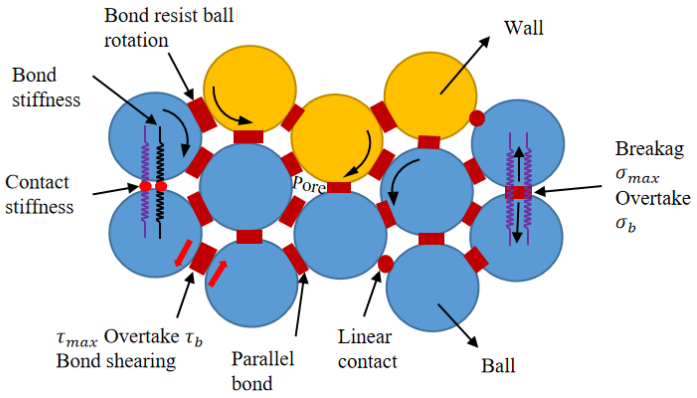

(a) The macrostructure

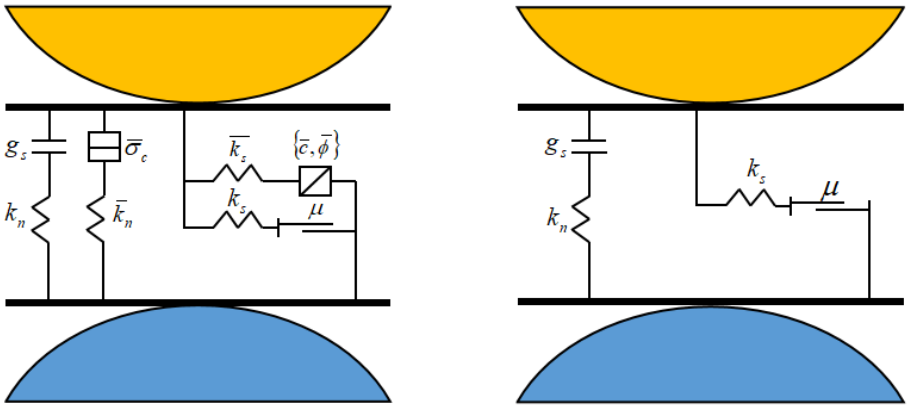

(b) The microstructure

Fig. 1 Parallel bond model

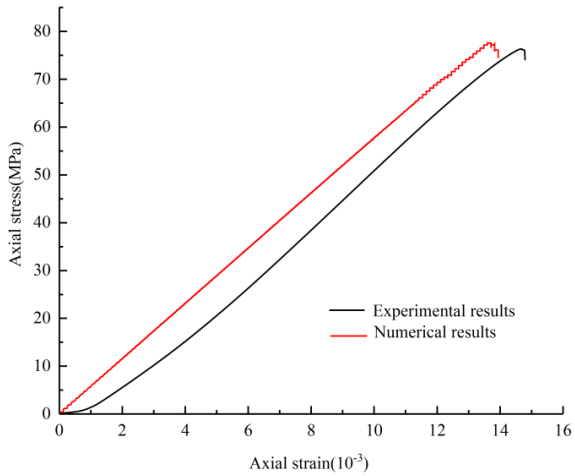

(a) Image contrast

Experimental result Simulation result

(b) Comparison between numerical simulation and experiment

Fig. 2 Comparison of the numerical results and test results

Table 1 Microscopic parameters used in the PFC2D model

Parameter	Value	Parameter	Value
Porosity	0.1	Minimum particle diameter	0.2
PB cohesive force (MPa)	47	Particle density (kg/m^3)	2500
Particle size ratio	1.4	Particle contact modulus (GPa)	3.3
PB tensile strength (MPa)	20	Friction angle of PB (º)	30

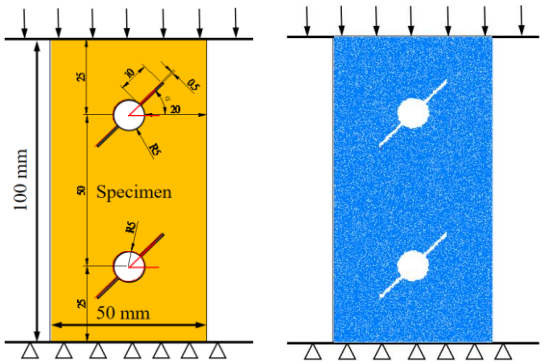

(a)Physical model (b)Numerical model

Fig. 3 Geometric parameters and numerical models of specimens

2.2 Establishment of the model

By using the PFC2D numerical simulation software, the mechanical properties and failure characteristics of double holes and fractures defect rocks with different dip angles were studied and numerical models of double holes and fractures rocks with different dip angles were established. The height of the models was 100 mm and the width was 50 mm. Each numerical model had two sets of the same hole-fracture combination defects located in the upper and lower parts of the model. The two sets of defects were parallel to each other. The hole radius was 5 mm, the whole area was 78.5 mm^2, and the fracture length was 30 mm. Numerical models with α = 0°, 15°, 30°, 45°, 60°, 75°, and 90° were established to study the angle α between the fracture and the horizontal line of the hole center. Similar to the laboratory physical test, uniaxial compression testing was conducted on the models with a loading rate of 0.01 mm/s axial velocity. The geometric parameters and geometric models of the rocks with double holes and fractures at different inclination angles are presented in Fig. 3.

3. Analysis of test results

3.1 Mechanical properties of rocks with different fracture angles

Fig. 4 presents the stress-strain curve and fracture-number-strain curve of the numerical models of rocks with double holes and fractures at different angles. Fig. 5 presents the stress-strain curve and fracture-number- strain curve of intact rocks. In Fig. 4, the color of the stress-strain curves and fracture-number-strain curves of rocks with the same fracture dip angles are the same. When comparing Figs. 4 and 5, one can see that the types of stress-strain curves and fracture-number strain curves of intact and defective rocks are similar. The stress-strain curves of intact rock and defective rock can be divided into four stages: the compaction stage, elastic stage, plastic stage, and failure stage. When the stress exceeded the peak stress, the stress decreased rapidly. The number of fractures in the intact rock and defective rock increased rapidly after reaching the peak stress, and the number of fractures increased gradually before reaching the peak stress.

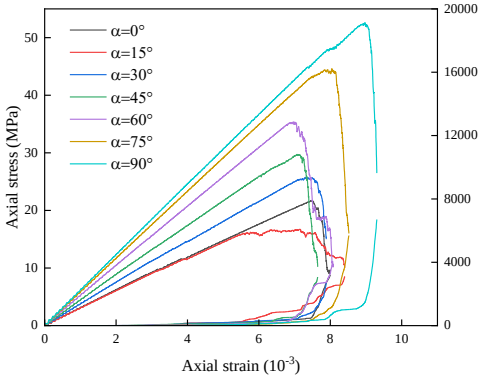

Fig. 4 Stress-strain curves and fracture-strain curves of rocks with different fracture inclination angles

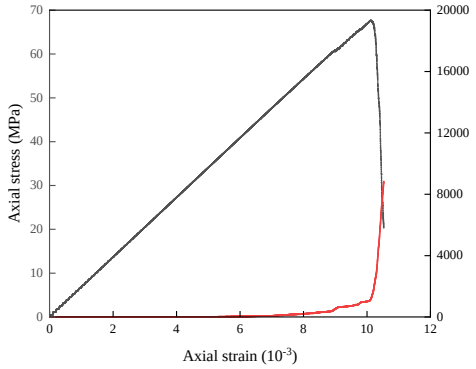

Fig. 5 Intact rock stress-strain curve and fracture-strain curve

The stress-strain curves of the complete rock numerical model and defective rock numerical model were different in terms of numerical magnitude. After reaching the peak stress, the stress drop rate of the defective rock numerical model with double holes and fractures was slower than that of the intact rock numerical model. This is because holes and fractures in the rock reduced the brittleness of the rock and increased the ductility of the defect numerical model. According to Fig. 4, the stress-strain curves and fracture-number-strain curves of rocks with double holes and fractures at different angles are different. The peak stress increased continuously from 0° to 90° for the defect angle because the fractures in the two groups of defects moved closer to each other with an increase in the angle and new

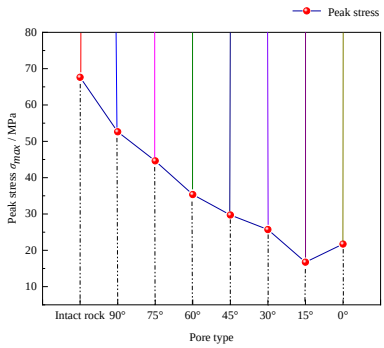

(a) Peak stress of the intact rock and fractured rock with different angles

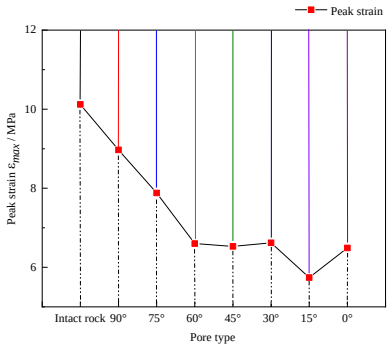

(b) Peak strain of the intact rock and fractured rock with different angles

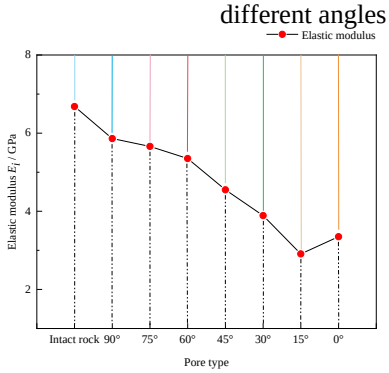

(c) Elastic modulus of the intact rock and fractured rock with different angles

Fig. 6 Mechanical parameters of intact rock and fractured rock with different angles

Table 2 Experimental parameters of intact rock, as well as double holes and fractures defect rock

Category	Peak stress/MPa	Peak strain/10^{-3}	Elastic modulus/GPa
α=0º	21.72	6.49	3.35
α=15º	16.73	5.74	2.91
α=30º	25.72	6.62	3.89
α=45º	29.73	6.53	4.55
α=60º	35.35	6.60	5.35
α=75º	44.62	7.88	5.66
α=90º	52.63	8.97	5.86
Intact rock	67.62	10.12	6.68

fractures were mainly developed from both ends of the initial fractures. Additionally, the larger the fracture angle, the faster the fracture development, and the sample model reached the peak stress earlier and the failure occurred earlier.

Figs 6(a)-6c) present the peak stress, peak strain, and elastic modulus, of the numerical models of intact rock and rock with double holes and fractures at different angles, respectively. For these three types of data, the numerical values of intact rock were greater than those of rock with double holes and fractures at different angles. In Fig. 6(a), one can see that the peak stress of the defective rock with a fracture angle between 90° and 15° exhibits a downward trend. Compared to the defective rock with a fracture angle of 15°, the peak stress of the defective rock with a fracture angle of 0° was slightly higher, but it did not exceed the peak stress of the defective rock with a fracture angle of 30°. In Fig. 6(b), one can see that the peak stress of defective rock with a fracture angle of 60° exhibits a downward trend, and the peak strain changes only a little when the fracture angle ranges from 60° to 15°, indicating that the change stage of the angle has little effect on the peak strain of the defective rock. In Fig. 6(c), it can be seen that the elastic modulus of intact rocks and defective rocks show an overall decreasing trend. Elastic modulus is minimum when fracture angle is 15° and maximum when fracture angle is 90°. Overall, with an increase in fracture angle, the gap in the mechanical properties between defect rock and intact rock gradually shrunk.

3.2 Determination of initiation stress and damage stress

By using PFC2D, uniaxial compression tests of rock samples with double holes and fractures with different angles were simulated and axial stress was gradually

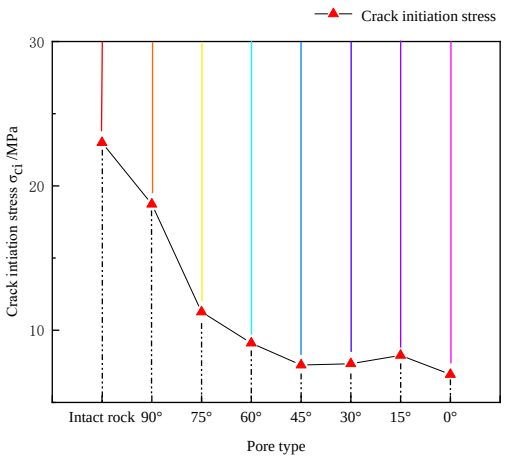

Fig. 7 Fracture initiation stress of the intact rock model and rock models with double holes and fractures with different angles

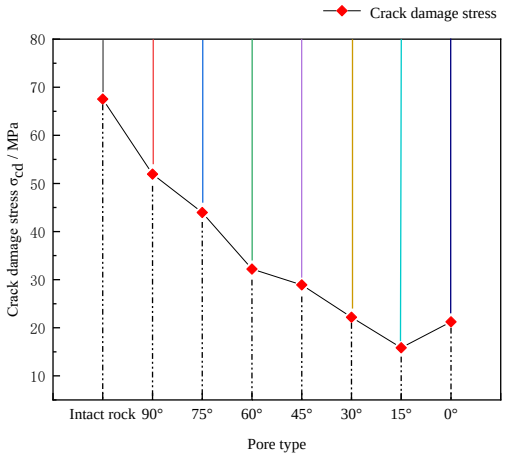

Fig. 8 Damage stress of the intact rock model and rock models with double holes and fractures with different angles

applied to the samples to explore their mechanical properties and failure characteristics. In the initial stage of applying pressure on the samples, the PBs between particles began to experience strain approaching their bond strength gradually and fractures began to appear in the samples. The corresponding axial stress is called the initiation stress. As the testing continued, the axial stress on the samples became increasingly larger, and the fracturing began to increase. The axial stress was about to reach its peak stress and the number of fractures began to increase rapidly; the corresponding stress is called the damage stress.

Crack initiation stress and damage stress are not only important characteristic values of rock strength but also demarcation points of different stages of crack propagation. Crack initiation stress indicates that the original cracks in the rock are compact and the new cracks start to initiate and expand, and the cracks are in a stable state at this time. However, the damage stress indicates that the microcracks initiated and expanded in the previous stage rapidly confluent and connected, which resulted in unstable propagation and finally reached the peak stress of rock. Therefore, it is of great significance to study the initiation stress and damage stress of rock for understanding the progressive failure process of rock and establishing the brittle failure mechanism, initiation strength, and long-term strength criterion.

As shown in Fig. 7, the fracture initiation stress values of rock models with double holes and fractures at different angles are less than that of the intact rock model. The fracture initiation stress of the rock models with fractures from 90° to 0° decreased gradually and only the fracture initiation stress of the rock model with fractures at 15° increased slightly. The damage stress of the intact rock model was greater than that of the defective rock models, and the damage stress of the defective rock models decreased with a decreasing fracture angle. The damage stress of the defective rock model with a fracture angle of 0° is greater than that of the fracture rock model with a fracture angle of 15°, as shown in Fig. 8. Considering Fig. 7 and 8, one can see that the initiation stress and damage stress of the intact rock model are greater than those of the rock models with double holes and fractures and that the difference generally decreases with a decreasing fracture angle. This is because the greater the fracture angle, the shorter the distance between the two fracture endpoints, which makes it easier for fractures to penetrate and develop. However, the fracture initiation stress of the defective rock with a fracture angle of 15° was relatively large and the damage stress was relatively small, indicating that the compaction time of the defective rock model with a fracture angle of 15° was relatively long, meaning that fracturing appeared slowly but develop rapidly after it appeared, and the rock model was destroyed.

4. Failure characteristics and stress evolution law of specimens

4.1 Failure characteristics of rock with double holes and fractures with different angles

From the PFC2D numerical simulation tests, the failure modes of the intact rock model and rock models with different angles of double holes and fractures are presented in Fig. 9. Most of the fractures generated when all models were destroyed were red tensile fractures, whereas yellow compression-shear fractures and green tensile-shear fractures were less common. The failure characteristics of intact rock models are different from those of the defective rocks, as shown in Fig. 9(a). The failure mode of the intact rock model considered that fractures began to develop from the lower-right side of the model and then developed toward the upper-left corner of the model until the model was destroyed. The failure mode was roughly hooked. The fractures in all defective rock samples began to develop at holes or fractures and continued to develop until they were broken. The failure modes of the defective rock samples with fracture angles of 0° and 15° were relatively similar. fractures began to develop from the upper and lower boundaries of the holes but developed slowly. With an increase in axial stress, the number of fractures began to increase rapidly and the fractures penetrated each other on

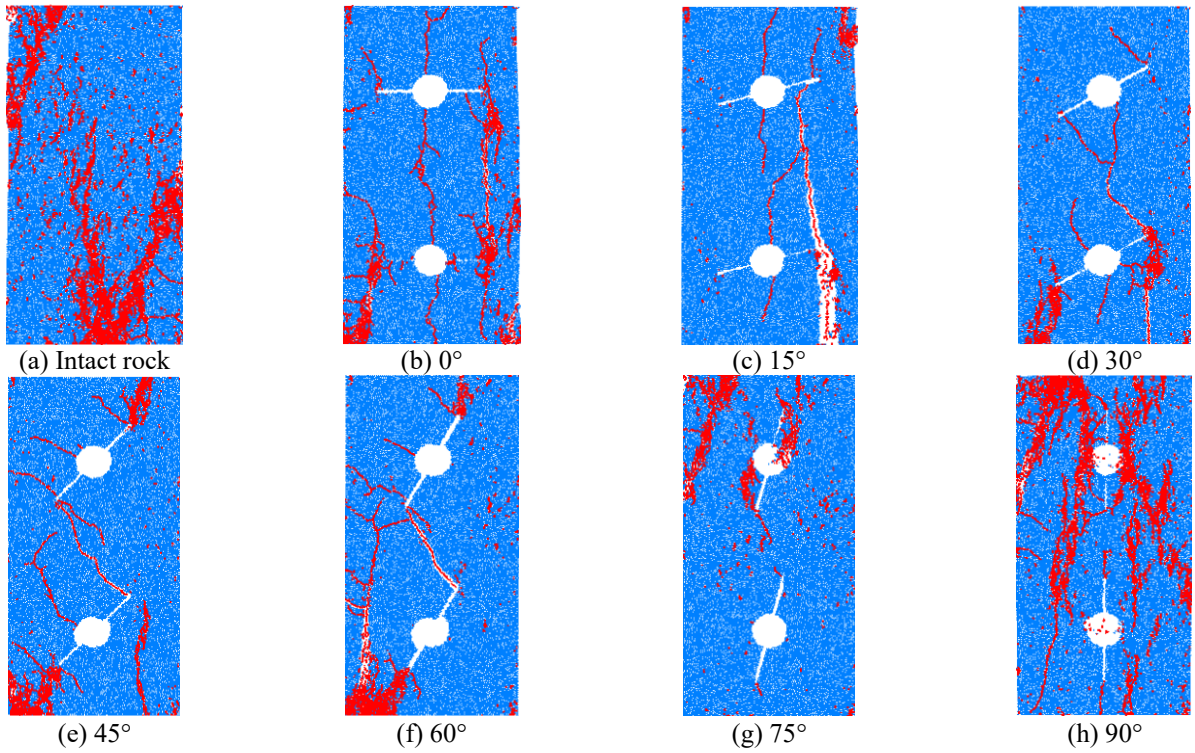

(a) Intact rock (b) 0° (c) 15° (d) 30°

(e) 45° (f) 60° (g) 75° (h) 90°

Fig. 9 Failure modes of the intact rock and fractured rock with different fracture angles around holes

the right side of the two initial fractures. However, the fractures generated at the right end of the fracture below the defect rock model with a fracture angle of 15° not only developed and penetrated into the upper fracture but also rapidly extended to the lower boundary of the specimen; thus, the specimen was destroyed earlier. This is also the reason the fracture initiation stress of the defective rock model with the fracture angle of 15° was large and its damage stress was small.

The failure modes of defective rock models with fracture angles of 30°, 45°, and 60° were similar. In the early stages of testing, fracturing began from both the ends of the initial fractures, and the fractures at the left end of the initial fractures developed downward, whereas the fractures on the right developed upward. The fracture at the left end of the upper fracture and the fracture at the right end of the lower fracture developed through the model, and the fracture at the left end of the lower fracture developed to the lower boundary of the model, resulting in shear failure at the location of the combined defects in the lower part of the model.

The fracture failure of the defective rock models with fracture angles of 75° and 90° was mainly concentrated in the upper half of the model. The fractures began to develop above the left side of the model and on the left side of the upper hole. After continuously loading axial stress onto the sample, the fractures on the upper part of the model and the left side of the hole developed and penetrated. Simultaneously, the fractures on the right side of the upper hole rapidly developed to the upper boundary of the model until the model was destroyed and the failure mode was a shear failure.

4.2 Fracture propagation and stress evolution of rocks with double holes and fractures defects at different angles

To study the stress distributions and evolution results of the intact rock and rock with double holes and fractures defects with different angles, the contact force chain and stress evolution results of the four stages of fracture initiation, damage, peak strain, and failure of each model were considered for analysis. In the contact force chain diagrams, the red region represents the tensile stress region and the blue region represents the compressive stress region. In the stress evolution results, tensile stress was positive and compressive stress was negative. The contact force chain and stress evolution results of the intact rock and rock with fractures at different angles around holes are presented in Fig. 10.

In Fig. 10, one can see that the intact rock model and rock models with double holes and fractures with different angles are dominated by compressive stress in the failure process and most failure in the defective rocks begins from the lower-left corners of the samples. Under the action of uniaxial compression, the rock specimens were damaged starting in the vicinity of defects, and the damage expanded to the upper and lower sides. The left end of the upper defect fracture and the right end of the lower defect fracture developed and penetrated into each other. When a defect rock model was subjected to stress loading, damage occurred near the holes and fractures, forming a tensile stress concentration area that developed along with the axial stress. Furthermore, the compressive stress concentration areas of holes and fractures began to develop gradually and the stress concentration range expand slowly. With a

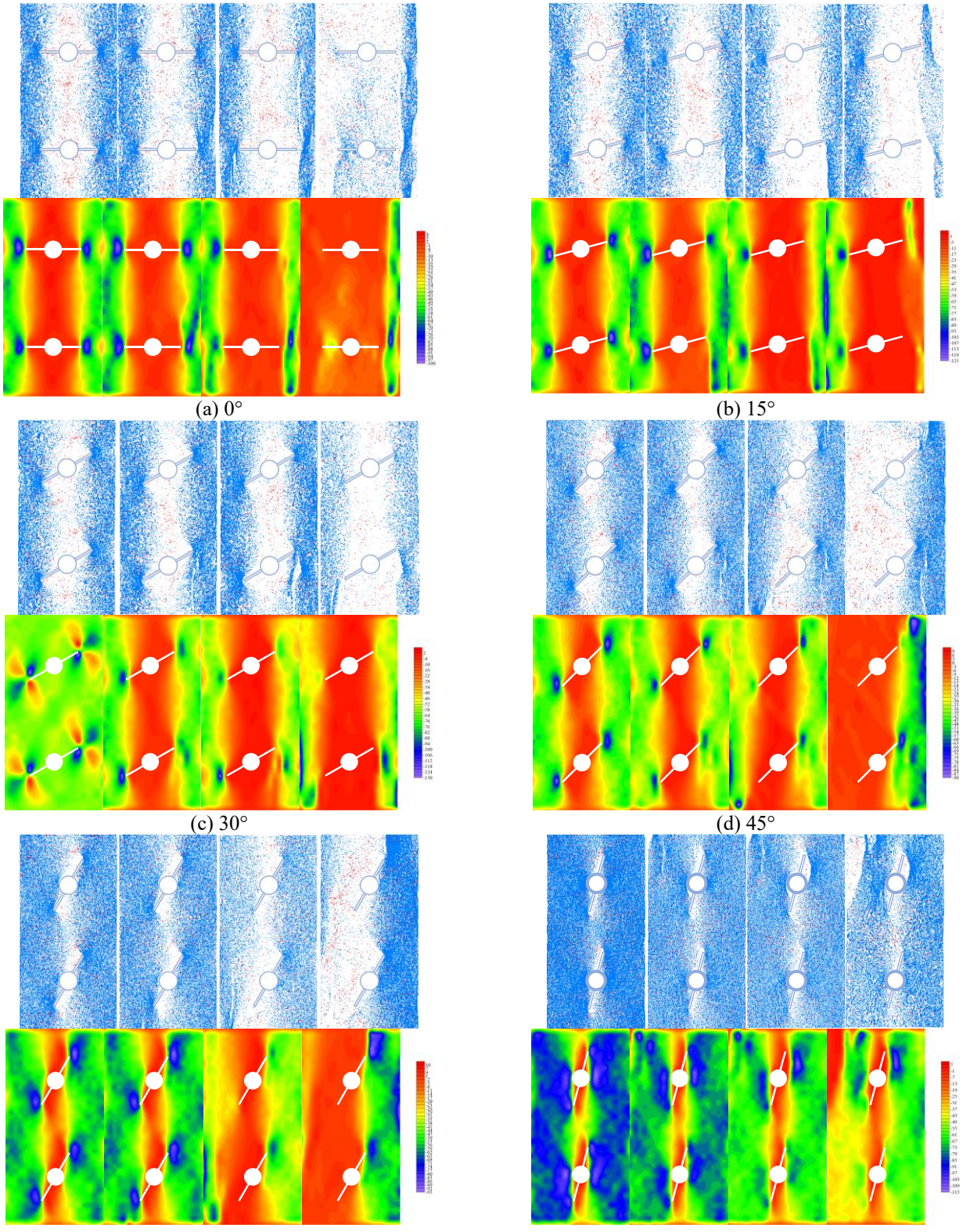

(a) 0° (b) 15°

(c) 30° (d) 45°

(e) 60° (f) 75°

Fig. 10 Contact force chain and stress evolution results of the intact rock and rock with fractures at different angles around holes

continuous increase in stress, the compressive stress concentration areas of the two upper and lower combined defects began to penetrate, the rock was destroyed, and the internal stress of the specimen was released in large quantities. In the force chain diagram, one can see that with a continuous increase in stress, the contact key of the compressive stress continuously breaks to form a tensile stress zone. The compressive stress concentration range of

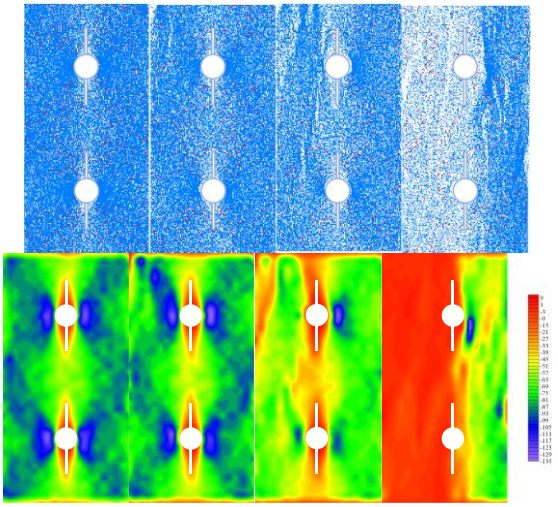

(g) 90°

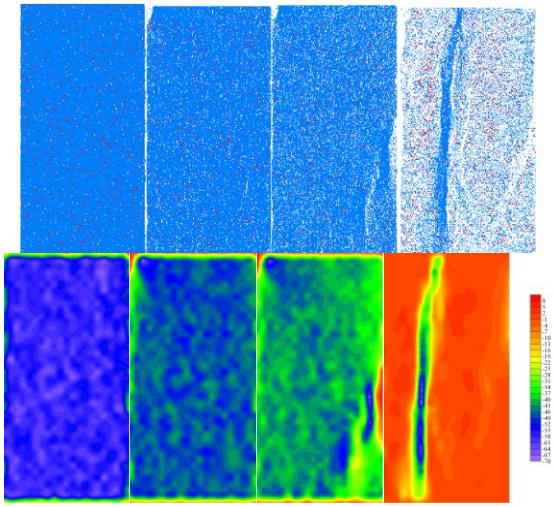

(h) Intact rock

Continued-

the combined defects of fractures and holes began to decrease, and the model was gradually destroyed as the tensile stress range gradually increased.

5. Laboratory test

5.1 Preparation and experimental process for test materials

The experimental material used in this study was red sandstone from Wuhan, Hubei. The main mineral components of red sandstone are clastic minerals and clay minerals. The detrital minerals are mainly quartz, feldspar, and calcite. The clay minerals include montmorillonite, illite, and kaolin. Based on the swelling of clay minerals in red sandstone, it is easily softened and destroyed after encountering water; therefore, it is difficult to prepare test samples. Therefore, only rock models with angles α of 30° and 45° between the horizontal line of the hole center and fracture were prepared for mechanical property testing to study the acoustic emission characteristics, fracture propagation, and digital speckle characteristics of rocks with different fracture angles. To reduce the influence of differences between specimens on the overall rock mechanical properties, all specimens were prepared from the same intact rock. The sample preparation process proceeded as follows. A complete rock was cut into several plate samples with a thickness of 20 mm. The plate samples were then cut into individual samples with a height of 100 mm, a width of 50 mm, and a thickness of 20 mm. The height-width ratio of the samples was 2:1. High-pressure water cutting machine was used to prefabricate holes and fractures in the samples. Two groups of hole-fracture combination defects were prefabricated in each sample and were in the upper and lower geometric areas of the samples, respectively. The geometric center distance of each hole from the upper and lower boundaries is 25 mm and the fracture length is 30 mm, as shown in Fig. 11.

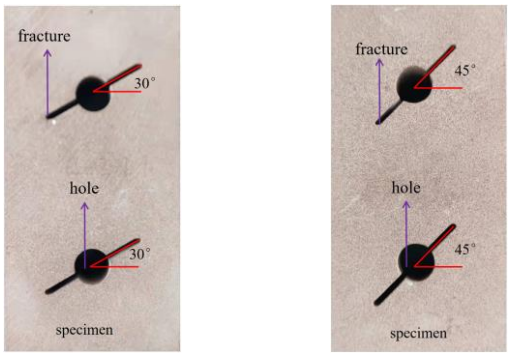

$\alpha = 30°$ $\alpha = 45°$

Fig. 11 Geometric shapes of double holes and fractures combined defects in our physical experiments

Our laboratory test equipment was the Shimadzu AG-X250 electronic universal testing machine. After a specimen was fixed, it was subjected to uniaxial compression at a loading rate of 0.01 mm/s axial velocity until the specimen was destroyed. During uniaxial compression, the acoustic emission signals and DIC digital characteristics of the rock are detected, as shown in Fig. 12.

5.2 Analysis of test results

According to Fig. 13, it can be observed that during the uniaxial compression testing of the defective rock, with a gradual increase in axial stress, the stress of the sample decreases rapidly after reaching the peak stress, and the acoustic emission energy collected by the sample increases rapidly to the maximum value when the stress reaches its peak. This is because red sandstone is a brittle rock when the stress exceeds the peak stress of the rock itself following rapid destruction. In the early stages of testing, the stress-strain curve exhibits nonlinear changes, mainly because there are many fine fractures in natural rock, which are gradually compacted under the action of axial stress. The stress-strain curve can be divided into an elastic stage, plastic stage, and failure stage in addition to the compaction stage. When the peak stress is reached, the acoustic emission energy is the highest and the rock is brittle.

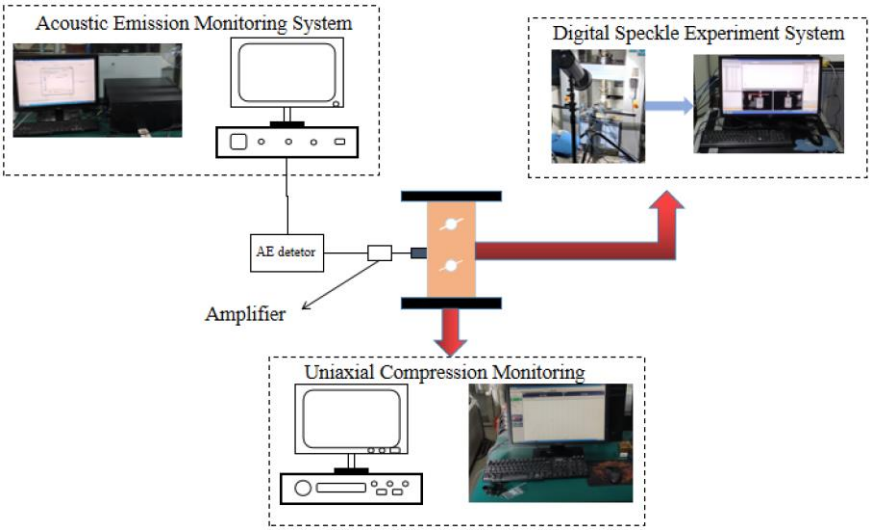

Fig. 12 Experimental setup and monitoring system

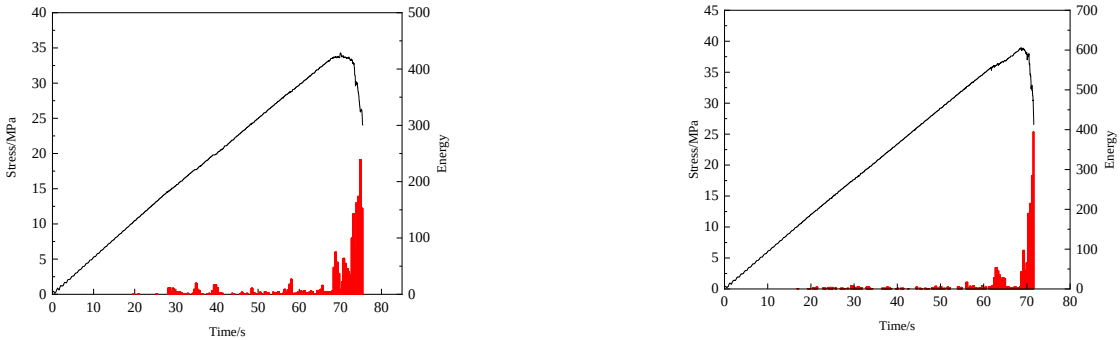

α = 30° (b) α = 45°

Fig. 13 Relationship between the axial stress-strain curve and acoustic emission times of the defective rock

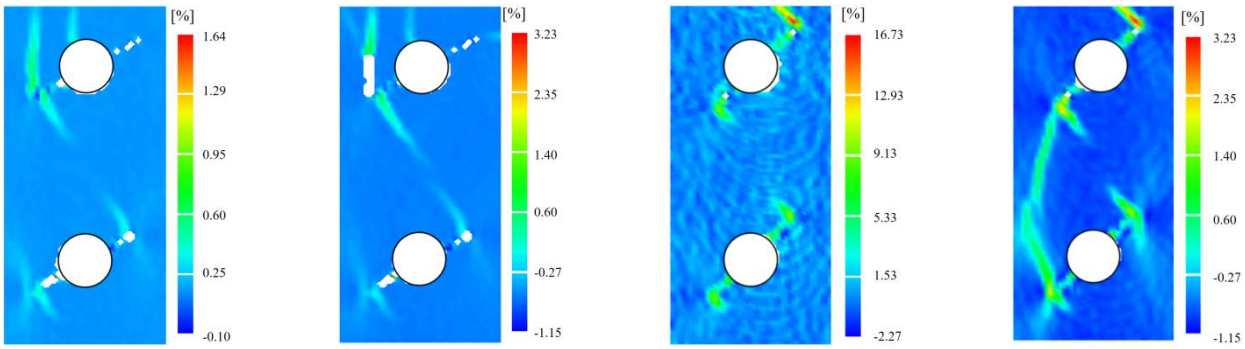

(a) α = 30° (b) α = 30° (c) α = 45° (d) α = 45°

Fig. 14 DIC numerical characteristics of rock fracture initiation and peak state in our physical experiments

Fig. 14 presents the DIC characteristics of double holes and fractures rock with fracture dip angles of 30° and 45° obtained through digital speckle testing. According to Fig. 14 and the stress-strain curves, acoustic emission times, and time relationship diagram, the failure characteristics of defective rock with dip angles of 30° and 45° were analyzed. When the fracture dip angle was 30°, the failure development process of rock specimens could be roughly divided into two stages. The first stage is the initiation of macroscopic fractures, as shown in Fig. 14(a). In this stage, with a gradual increase in axial stress, some fine fractures began to appear at both ends of the fracture and around the hole. The stress-strain curve exhibited nonlinear changes that are accompanied by a small amount of acoustic emission energy. The next stage was fracture coalescence development. With a continuous increase in axial stress, the fractures on the surface and inside of the rock specimen gradually grew. The fractures generated by the two groups of defects begin to penetrate each other and the fractures begin to develop to the specimen boundary, as shown in

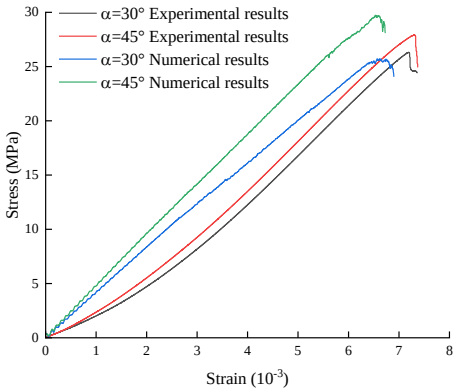

Fig. 15 Comparison of axial stress-strain curves between laboratory tests and numerical simulation tests

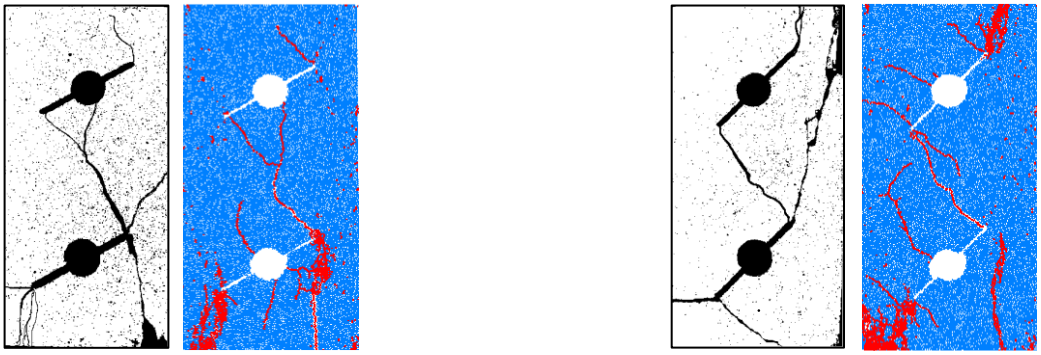

(a) α = 30° (b) α = 45°

Fig. 16 Failure diagram of laboratory tests and numerical simulation tests with fracture angles of 30° and 45°

Fig. 14(b). Finally, in the rock failure stage, after reaching the peak stress, the fractures in the rock sample rapidly developed and grew, and the acoustic emission energy value instantly increased.

When the fracture dip angle was 45°, the failure characteristics of rock samples were roughly the same as those described above. The failure process was also divided into three stages macro fracture initiation, fracture penetration, and rock failure. In the macro fracture initiation stage, the internal fractures in the rock sample were compacted and fine fractures began to appear at both ends of the fracture and around the hole. In the fracture coalescence stage, the fractures around the initial fracture and hole grew and penetrated, and the fractures between the two groups of defects developed and penetrated each other, eventually expanding to the boundary of the specimen. The failure stage occurred after the peak stress was reached, and the acoustic emission energy increased rapidly.

After the PFC2D numerical simulation tests were completed, the data were compared to the laboratory tests data. In Figs. 15 and 16, one can see that the stress-strain curves and failure modes of the model are similar between the two tests. In Fig. 15, the black and red curves are the stress-strain curves from the laboratory tests of the defect rocks with fracture angles of 30° and 45°, respectively. The blue and green curves are the stress-strain curves of the numerical simulation tests of the defect rocks with fracture angles of 30° and 45°, respectively. Although there were differences in peak strain, these differences were attributed to the compaction area of the stress-strain curves obtained in the laboratory tests. Overall, the parameter variable values were acceptable.

The failure characteristics of the laboratory tests and numerical simulation tests of the defective rocks with fracture angles of 30° and 45° are presented in Fig. 16. In Fig. 16, one can see that the fracture development in the process of the laboratory experiment and numerical experiment begins from the vicinity of the defects. The fractures at the ends of the upper and lower initial fractures developed and penetrated into each other and then developed and expanded to the left side of the specimen. It can be observed that the macroscopic failure characteristics of the real rock specimen and numerical specimen were roughly similar when the fracture defect angles were 30° and 45°.

Based on the comparison of the axial stress-strain curves between the laboratory tests and the numerical simulation tests in Fig. 15, it can be observed that the peak strengths of the real rock with defect angles of 30° and 45° are 26.30 MPa and 27.90 MPa, respectively, whereas the numerical simulation results are 25.72 MPa and 29.73 MPa, respectively. The strength errors between the laboratory tests and numerical simulations were relatively small. Overall, the numerical experiments agreed well with the strength and deformation parameters of real rock specimens, meaning they could reflect the strength and deformation characteristics of the rock.

6. Conclusions

In this paper, we conducted numerical simulation research on rock mechanical properties, fracture propagation, and stress field evolution for combined defects of double holes and fractures with different angles using the PFC2D software. A comparative analysis was conducted between laboratory real rock experiments and numerical simulation experiments, and the following conclusions were obtained.

(1) The combined defects of double holes and fractures at different angles had a significant influence on the mechanical properties of rock. The peak strength, peak strain, elastic modulus, fracture initiation stress, and damage stress of rock with double holes and fractures at different angles were significantly smaller than the corresponding mechanical parameters of intact rock.

(2) The combined defects of double holes and fractures at different angles had an obvious influence on the failure characteristics of rock samples. The fracture initiation of defective rocks was generated from fracture tips or around holes. The distribution of the combined defects of double holes and fractures at different angles caused different fracture development and propagation processes. Both tensile and compressive stress concentration regions were generated following the uniaxial compression of the defective rock, which was dominated by compressive stress concentrations. The concentration regions were mainly distributed around holes and fractures, as well as on the lower-left boundary of a rock sample.

(3) Through a comparative study, it was determined that the results of laboratory rock physical tests and numerical simulation tests were in good agreement and the macroscopic failure characteristics of rocks were similar, demonstrating the accuracy of PFC2D numerical simulation tests.

(4) Through laboratory tests and numerical simulation tests, the mechanical properties and failure characteristics of the rock with double holes and fractures at different angles were analysed. These research results of the fracture behavior of existing fractured rock mass can promote the development of fractured rock mass mechanics and increase the understanding of the instability and failure mechanism of rock engineering such as nuclear waste disposal engineering and deep underground engineering.

Data Availability

The data used to support the findings of this study are included within the article.

Conflicts of Interest

The authors declare that there are no conflicts of interest regarding the publication of this paper.

Acknowledgements

This work was supported by National Natural Science Foundation of China (52004146, 52074169, 52174159, 51904167); Natural Science Fundation Youth Branch of Shandong Province (ZR2020QE102); the Research Fund of Key Laboratory of Deep Coal Resource Mining (CUMT), Ministry of Education (KLDCRM202102); the 2020 Joint Fund for the Project of the State Key Laboratory of Coal Resources and Safe Mining- Outstanding Young Scientists Program of Beijing Higher Education Institutions (SKLCRSM20LH04) and SDUST Research Fund (2019TDJH101).

References

Bahaaddini, M. and Sharrock, G. (2013), "Numerical investigation of the effect of joint geometrical parameters on the mechanical properties of a non-persistent jointed rock mass under uniaxial compression", *Comput. Geotech*., **49**, 206-225. https://doi.org/10.1016/j.compgeo.2012.10.012.

Chen, S., Xia, Z., Feng, F. and Yin, D. (2020), "Numerical study on strength and failure characteristics of rock samples with different hole defects", *B Eng Geol Environ.*, **80**(7), 1-18. https://doi.org/10.1007/s10064-020-01964-y.

Cho, N., Martin, C.D. and Sego, D.C. (2007), "A clumped particle model for rock", *Int. J. Rock Mech. Min.*, **44**(7), 997-1010. https://doi.org/10.1016/j.ijrmms.2007.02.002.

Chung, J., Lee, H. and Kwon, S. (2019), "Numerical investigation of radial strain-controlled uniaxial compression test of äspö diorite in grain-based model", *Rock Mech. Rock Eng*., **52**(10), 3659–3674. https://doi.org/10.1007/s00603-019-01838-0.

Cundall, P.A. and Strack, O.D. (1979), "A discreate numerical model for granula assemblies", *Geotechnique*., **29**(1), 47-65. https://doi.org/10.1680/geot.1979.29.1.47.

Estrada, J.M. and Bhamidimarri, R. (2016), "A review of the issues and treatment options for wastewater from shale gas extraction by hydraulic fracturing", *Fuel.*, **182**, 292-303. https://doi.org/10.1016/j.fuel.2016.05.051.

Li, D., Han, Z., Sun, X., Zhou, T. and Li, X. (2018), "Dynamic mechanical properties and fracturing behavior of marble specimens containing single and double flaws in shpb tests", *Rock Mech. Rock Eng*., **52**(6), 1623-1643. https://doi.org/10.1007/s00603-018-1652-5.

Li, J., Zhou, Y., Sun, W. and Sun, Z. (2019), "Effect of the interaction between cavities and flaws on rock mechanical properties under uniaxial compression", *Adv. Mater. Sci. Eng.*, **2019**, 1-9. https://doi.org/10.1155/2019/1242141.

Li, K.G., Yang, B.W. and Li, X.X. (2017), "Effect of native fissures on the mechanical behaviour of rock under uniaxial compression", *Teh Vjesn*., **24**(3), 907-915. https://doi.org/10.17559/TV-20170523104531.

Li, R., Wang, Y.S. and Fu, F.F. (2019), "Research on fatigue damage and affecting factors of defected rock mass based on ultrasonic wave velocity", *The. Vjesn.*, **26**(4), 1061-1067. https://doi.org/10.17559/TV-20190228065832.

Lisjak, A. and Grasselli, G. (2014), "A review of discrete modeling techniques for fracturing processes in discontinuous rock masses", *J. Rock Mech. Geotech.*, **6**(4), 301-314. https://doi.org/10.1016/j.jrmge.2013.12.007.

Mohammadi, M. and Tavakoli, H. (2015), "Comparing the generalized Hoek-Brown and Mohr-Coulomb failure criteria for stress analysis on the rocks failure plane", *Geomech. Eng*., **9**(1), 115-124. https://doi.org/10.12989/gae.2015.9.1.115.

Nicksiar, M. and Martin, C.D. (2014), "Factors Affecting Crack Initiation in Low Porosity Crystalline Rocks", *Rock Mech. Rock Eng*., **47**(4), 1165-1181. https://doi.org/10.1007/s00603-013-0451-2.

Tan, Y., Cheng, H., Gong, S., Bai E.H., Shao M.C., Hao, B.Y., Li,

X.S. and Xu, H. (2021), "Field study on the law of surface subsidence in the high-intensity fully mechanized caving mining working face with shallow thick bedrock and thin epipedon in hilly areas", *Adv. Mater. Sci. Eng.*, **2021**, 13. https://doi.org/10.1155/2021/6515245.

Tan, Y., Xu, H., Yan, W.T., Guo, W.B., Bai, E.H., Qi, T.Y., Yin, D.W., Hao, B.Y., Cheng, H. and Shao, M.H. (2022), "Study on the overburden failure law of high-intensity mining in gully areas with exposed bedrock", *Front Earth Sc-Switz.*, **10**, 833384. https://doi.org/10.3389/feart.2022.833384.

Tan, Y., Xu, H., Yan, W.T., Guo, W.B., Sun, Q., Yin, D.W., Zhang, Y.J., Zhang, X.Q., Jing, X.F., Wei. S.J. and Liu, X. (2022), "Development law of water conducting fracture zone in the fully mechanized caving face of gob-side entry driving: A case study", *Minerals-Basel*, **12**:557. https://doi.org/10.3390/min12050557.

Usol'Tseva, O.M. and Tsoi, P.A. (2021), "The influence of size effect on strength and deformation characteristics of different types of rock samples", *Environ. Earth Sci*., **720**(1), 12-89. https://doi.org/10.1088/1755-1315/720/1/012089.

Wang, C., Zhang, S., Zhang, B., Sun, J. and Chen, L. (2020), "Failure characteristics and physical signals of jointed rock: an experimental investigation", *Arab. J. Geosci.,* **13**(14). https://doi.org/10.1007/s12517-020-05675-2.

Wang, C.X., Shen, B.T., Chen, J.T., Tong, W.X., Jiang, Z., Liu, Y. and Li, Y.Y. (2020), "Compression characteristics of filling gangue and simulation of mining with gangue backfilling: An experimental investigation", *Geomech. Eng*., **20**(6), 485-495. https://doi.org/10.12989/gae.2020.20.6.485.

Wang, J., Apel, D.B., Dyczko, A., Walentek, A., Prusek, S., Xu, H., and Wei, C. (2021), "Investigation of the rockburst mechanism of driving roadways in close-distance coal seam mining using numerical modeling method", *Min. Metall. Explor,* **38**(5), 1899-1921. https://doi.org/10.1007/s42461-021-00471-2.

Wang, J., Apel, D.B., Pu, Y., Hall, R., Wei, C. and Sepehri, M. (2021), "Numerical modeling for rockbursts: A state-of-the-art review", *J. Rock Mech. Geotech.*, **13**(2), 457-478. https://doi.org/10.1016/j.jrmge.2020.09.011.

Wang, X. and Tian, L.G. (2018), "Mechanical and crack evolution characteristics of coal-rock under different fracture-hole conditions: a numerical study based on particle flow code", *Environ. Earth Sci.*, **77**(8), 297. https://doi.org/10.1007/s12665-018-7486-3.

Wang, X., Wen, Z.J. and Jiang, Y.J., (2016), "Time-space efect of stress feld and damage evolution law of compressed coal-rock", *Geotech. Geol. Eng.,* **34**(6), 1933-1940. https://doi.org/10.1007/s10706-016-0074-y.

Wang, X.F., Xia, Z.G., Li, P. and Liu, H.N. (2021), "Numerical study on strength and failure behavior of rock with composite defects under uniaxial compression", *Energies*., **14**(15). https://doi.org/10.3390/en14154418.

Wei, Z., Yang, S.Q. and Tian, W.L. (2018), "Experimental and numerical investigation of brittle sandstone specimens containing different shapes of holes under uniaxial compression", *Eng. Fract. Mech.*, **200**, 430-450. https://doi.org/10.1016/j.engfracmech.2018.08.016.

Wu, T.H., Gao, Y.T., Zhou, Y. and Li, J.W. (2020), "Experimental and numerical study on the interaction between holes and fissures in rock-like materials under uniaxial compression", *Theor. Appl. Fract. Mech.*, **106**. https://doi.org/10.1016/j.tafmec.2020.102488.

Yin, D.W., Chen, S.J., Sun, X.Z. and Jiang, N. (2021), "Effects of interface angles on properties of rock-cemented coal gangue-fly ash backfill bi-materials", *Geomech. Eng.*, **24**(1), 81-89. https://doi.org/10.12989/gae.2021.24.1.081.

Zhang, Q., Wang, X., Tian, L.G. and Huang, D.M. (2018), "Analysis of mechanical and acoustic emission characteristics of rock materials with double-hole defects based on particle flow code", *Shock Vib.*, **2018**(9), 1-11. https://doi.org/10.1155/2018/7065029.

Zhao, T.B., Guo, W.Y., Liu, C.P. and Zhao, G.M. (2016), "Failure characteristics of combined coal-rock with different interfacial angles", *Geomech. Eng.*, **11**(3), 345-359. https://doi.org/10.12989/gae.2016.11.3.345.

Zhu, D., Jing, H.W., Yin, Q., Zong, Y.J. and Tao, X.L. (2018), "Experimental study on mechanical characteristics of sandstone containing arc fissures", *Arab. J. Geosci.*, **11**(20), 1-10. https://doi.org/10.1007/s12517-018-3991-7.

Zhu, J.B., Zhou, T., Liao, Z.Y., Sun, L., Li, X.B. and Chen, R. (2018), "Replication of internal defects and investigation of mechanical and fracture behaviour of rock using 3d printing and 3d numerical methods in combination with x-ray computerized tomography", *Int. J. Rock Mech. Min.*, **106**, 198-212. https://doi.org/10.1016/j.ijrmms.2018.04.022.

GC